

Chapter 13

Water Nanodroplets: Molecular Drag and Self-assembly

J. Russell, B. Wang, N. Patra, and P. Král

Abstract Directed transport and self-assembly of nanomaterials can potentially be facilitated by water nanodroplets, which could carry reactants or serve as a selective catalyst. We show by molecular dynamics simulations that water nanodroplets can be transported along and around the surfaces of vibrated carbon nanotubes. We show a second transport method where ions intercalated in carbon and boron-nitride nanotubes can be solvated at distance in polarizable nanodroplets adsorbed on their surfaces. When the ions are driven in the nanotubes by electric fields, the adsorbed droplets are dragged together with them. Finally, we demonstrate that water nanodroplets can activate and guide the folding of planar graphene nanostructures.

J. Russell

Materials Science Division, Argonne National Laboratory, 9700 Cass Ave Bldg
200 Argonne, IL 60546, USA
e-mail: jrussell@anl.gov

B. Wang

Institute of Chemistry, Chinese Academy of Science, Beijing, China
e-mail: wangby@itp.ac.cn

N. Patra

Department of Chemistry, University of Illinois at Chicago, 845 W. Taylor
St. Rm 4500 SES, Chicago, IL 60546, USA
e-mail: npatra2@uic.edu

P. Král (✉)

Department of Chemistry, University of Illinois at Chicago, 845 W. Taylor
St. Rm 4500 SES, Chicago, IL 60546, USA

Department of Physics, University of Illinois at Chicago, 845 W. Taylor
St. Rm 4500 SES, Chicago, IL 60546, USA
e-mail: pkral@uic.edu

13.1 Introduction

Molecular transport and self-assembly of nanomaterials have important applications in medicine, nanofluidics, and molecular motors. Nanocarbons, such as carbon nanotubes (CNTs) and graphene, have many useful properties which make them attractive supports for directed molecular transport. CNTs [1] can serve as nanoscale railroads for transport of materials, due to their linear structure, mechanical strength, slippery surfaces, and chemical stability [2]. For example, electric currents passing through CNTs can drag atoms/molecules intercalated/adsorbed on CNTs [3–5]. Polar molecules and ions adsorbed on CNT surfaces can also be dragged by ionic solutions passing through the tubes [6–8]. Recently, nanoparticles [9, 10] and nanodroplets [11, 12] have been dragged along CNTs by hot phonons in thermal gradients. Analogously, breathing [13] and torsional [14] coherent phonons can pump fluids inside CNTs. In this chapter, we explore drag phenomena of nanodroplets on CNTs by vibrations [15] and by coupling to distantly solvated ions [16]. We also investigate droplet-driven self-assembly where nanodroplets guide the folding of planar graphene nanostructures [17].

13.2 Methods

We simulate water nanodroplets on graphene and CNT supports with classical molecular dynamics simulations, using NAMD [18], with the CHARMM27 force field [19], and VMD [20] for visualization and analysis. We estimate parameters of atoms in aliphatic groups and the graphitic support from similar atom types or calculate them ab initio [21], and add them to the force field. The nanodroplets couple to the CNT or graphene support by van der Waals (vdW) forces, described in CHARMM with the Lennard-Jones potential energy [22]

$$V_{\text{LJ}}(r_{ij}) = \varepsilon_{ij} \left[\left(\frac{R_{\text{min},ij}}{r_{ij}} \right)^{12} - 2 \left(\frac{R_{\text{min},ij}}{r_{ij}} \right)^6 \right]. \quad (13.1)$$

Here, $\varepsilon_{ij} = \sqrt{\varepsilon_i \varepsilon_j}$ is the depth of the potential well, $R_{\text{min},ij} = \frac{1}{2}(R_{\text{min},i} + R_{\text{min},j})$ is the equilibrium vdW distance, and r_{ij} is the distance between a CNT or graphene atom and a water atom.

In order to make sure our CNT and graphene models can be quantitatively matched to experiments, we calculate the flexural rigidity D of our graphene sheets and compare it with theoretical results [23–25]. We simulate a graphene sheet with the size of $a \times b = 3.7 \times 4.0 \text{ nm}^2$, which is rolled on to a cylinder with the radius of $R = a/2\pi$; we use the CHARMM27 force field parameters $k_{\text{bond}} = 322.55 \text{ kcal}/a^2$, $k_{\text{angle}} = 53.35 \text{ kcal}/\text{mol}\text{-rad}^2$ and $k_{\text{dihedral}} = 3.15 \text{ kcal}/\text{mol}$. From the simulations, we

calculate the energy associated with the cylindrical deformation of the graphene sheet, to obtain its strain energy density σ_{ela} . This allows us to calculate the flexural rigidity D , by using the formula $\sigma_{\text{ela}} = \frac{1}{2} D \kappa^2$, where $\kappa = 1/R$ is valid in the linear elastic regime [26]. The obtained value of $D = 0.194 \text{ nN nm}$ (27.9 kcal/mol) is in close agreement with ab initio results, $D_1 = 0.238 \text{ nN nm}$ [24], and other model studies, giving $D_2 = 0.11 \text{ nN nm}$ [25] and $D_3 = 0.225 \text{ nN nm}$ [26]. Therefore, our simulations should be reasonably close to potential experiments.

13.3 Nanodroplet Transport on Vibrated Nanotubes

Materials adsorbed on macroscopic solid-state surfaces can be transported by surface acoustic waves (SAW) [27]. This method has many practical applications, such as conveyor belt technologies [28], ultrasonic levitation of fragile materials [29], slipping of materials on tilted surfaces [30, 31], threading of cables inside tubes [32], and droplet delivery in microfluidics [33–37].

In this section, we examine the possibility of using SAW at the nanoscale. We use classical molecular dynamics (MD) simulations to model dragging of water nanodroplets on the surface of CNTs by coherent acoustic waves. Such coherent vibrations might be generated by piezo-electric generators [38, 39]. In analogy to coherent control of molecules by light [40], specialized pulses of coherent phonons might also be used in precise manipulation of materials.

13.3.1 Model System

Our model systems are formed by nanodroplets consisting of a number, N_w , of water molecules adsorbed at $T = 300 \text{ K}$ on the (10,0) CNT, and transported along/around its surface by coupling to coherent transversal acoustic (TA) phonon waves, as shown in Fig. 13.1.

The edge atoms at one of the ends of the 450 nm long CNT are fixed. At this end the tube is also oscillated. To prevent the CNT translation, four dummy atoms are placed in its interior at both ends. Otherwise, the tube is left free. A small Langevin damping [41] of 0.01 ps^{-1} is applied to the system to continuously thermalize it, while minimizing the unphysical loss of momenta [6]; the time step is 2 fs. At the two CNT ends, two regions with high damping of 10 ps^{-1} are established to absorb the vibrational waves. One region (35 nm long) is close to the generation point, and the other (180 nm long) is at the other CNT end. We model the systems in a NVT ensemble (periodic cell of $15 \times 15 \times 470 \text{ nm}^3$).

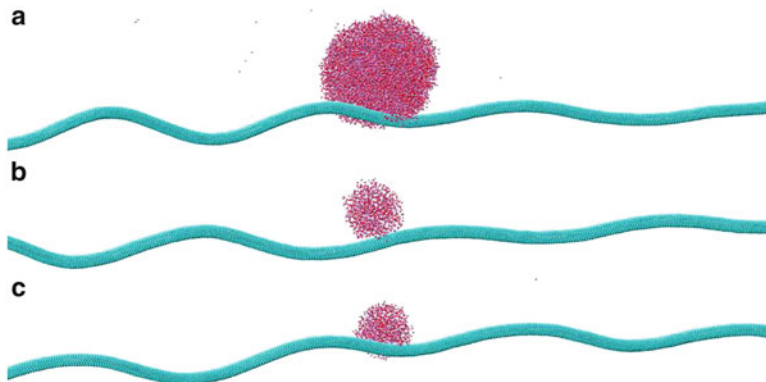


Fig. 13.1 Nanodroplets of (a) $N_w = 10,000$ and (b) $N_w = 1,000$ waters adsorbed on the (10,0) CNT and dragged by the linearly polarized TA vibrational wave with the amplitude of $A = 1.2$ ($T = 300$ K). (c) A nanodroplet of $N_w = 1,000$ adsorbed on the same CNT is dragged by a circularly polarized vibrational wave of $A = 0.75$ nm

13.3.2 Nanodroplet Transport by Linearly Polarized Waves

The vibrational waves are generated at one CNT end by applying a periodic force (orthogonal to its axis), $F = F_0 \sin(\omega t)$, on the carbon atoms separated 35–40 nm from the CNT end. This generates a linearly polarized TA vibration wave, $A_y(t) = A \sin(\omega t)$, where $\omega \approx 208$ GHz, $k = 2\pi/\lambda \approx 0.157$ nm⁻¹, and $A \approx 0.3$ –2.1 nm for $F_0 = 0.6948$ –5.558 pN/atom. The TA waves propagate along the nanotube with the velocity of $v_{vib} = \omega/k \approx 1,324$ nm/ns, scatter with the nanodroplet, and become absorbed at the tube ends. In our simulations, we let the wave pass around the droplet for a while and then evaluate its average steady-state translational, v , and angular, ω_d , velocities.

In Fig. 13.2, we show the (linear) velocities of nanodroplets with $N_w = 1,000$ and 10,000 water molecules in dependence on the vibrational amplitude, A . The data are obtained by averaging the droplet motion over trajectories of the length of $t \approx 7.2$ ns. We can see that the 10-times smaller droplet moves about 15-times faster for the same driving conditions. At small amplitudes, $A < 1.2$ nm, the velocities roughly depend quadratically on the driving amplitude. At larger amplitudes, $A > 1.2$ nm, they gain a linear dependence.

The nanodroplet is transported by absorbing a momentum from the vibrational wave. Its steady-state motion is stabilized by frictional dissipation of the gained momentum with the nanotube, which carries it away through the highly damped and fixed atoms. In the first approximation, the droplet motion might be described by the Boltzmann equation. In the steady state, obtained when a wave of a constant amplitude is passed through the CNT, the momentum of the droplet averaged over a short time (50 ps) is constant. Then, the constant driving force acting on the droplet, \dot{P}_{drive} , is equal to the friction force, $\dot{P}_{friction}$, between the droplet and the CNT [22] (linear motion—vectors omitted),

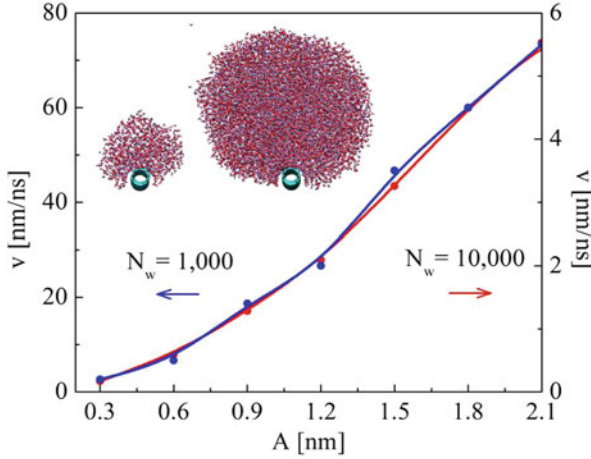


Fig. 13.2 The drag velocity of nanodroplets with $N_w = 1,000$ and $10,000$ waters in dependence on the amplitude, A , of the linearly polarized wave, with the frequency of $\omega = 208$ GHz. (inset) The adsorbed nanodroplets viewed in the CNT axis

$$\begin{aligned}\dot{P}_{\text{drive}} &= \int p F(r) \frac{\partial f}{\partial p} dr dp \\ &= \int p \left(\frac{\partial f}{\partial t} \right)_{\text{coll}} dr dp = \dot{P}_{\text{friction}}.\end{aligned}\quad (13.2)$$

Here, $f(r, p)$ is the position and momentum distribution function of the waters in the nanodroplet (normalized to N_w) and $F(r)$ is the force acting on each of the waters at r . The collision term $\left(\frac{\partial f}{\partial t}\right)_{\text{coll}}$ describes scattering of waters with each other and the CNT, where the last option causes the droplet to relax its momentum [42]. In the approximation of the momentum relaxation time [43], τ_p , the damping term can be described as,

$$\int p \left(\frac{\partial f}{\partial t} \right)_{\text{coll}} dr dp = \int p \frac{f - f_0}{\tau_p} dr dp \approx \frac{P_{\text{droplet}}}{\tau_p}, \quad (13.3)$$

where P_{droplet} is the steady-state average momentum of the nanodroplet [6, 7].

As the acoustic wave propagates along the CNT, it carries the momentum density [44],

$$g(t, x) = \mu \omega k A^2 [1 + \cos(2kx - 2\omega t)], \quad (13.4)$$

where μ is the CNT mass per unit length and the other symbols are the same as before. Assuming, for simplicity, that the momentum density of the wave is fully passed to the droplet (only approximately true, as seen in Fig. 13.1), we obtain

$$\dot{P}_{\text{drive}} = \frac{1}{2} \mu \omega^2 A^2 = \frac{P_{\text{droplet}}}{\tau_p}. \quad (13.5)$$

Equation 13.5 shows that the droplet velocity scales as

$$v_t = \frac{P_{\text{droplet}}}{m} \approx \frac{A^2 \tau_p}{m}. \quad (13.6)$$

Moreover, the momentum relaxation time, $\tau_p \approx S^{-1}$, can be assumed to scale inversely with the contact area, S , between the droplet and the CNT, due to friction. The 15 times larger velocity of the 10 times smaller droplet with a smaller contact area matches our expectations from (13.6). The quadratic dependence of the droplet velocities on the driving amplitude, A , shown in Fig. 13.2, also roughly agrees with (13.6).

13.3.3 Nanodroplet Transport by Circularly Polarized Waves

Next, we simulate transport of nanodroplets with $N_w = 1,000$ and $2,000$ waters, adsorbed on the (10,0) CNT, by circularly polarized TA waves. Application of the force of $\mathbf{F}(t) = (F_x, F_y) = F_0(\sin(\omega t), \cos(\omega t))$, $F_0 = 0.4864 - 2.084$ pn/atom, on the same C atoms as before generates a circularly polarized wave, $\mathbf{A}(t) = (A_x, A_y) = A(\sin(\omega t), \cos(\omega t))$, where $A \approx 0.21 - 0.75$ nm, $\omega \approx 208$ GHz, and $k \approx 0.157$ nm $^{-1}$. The circularly polarized TA waves carry both linear and angular momenta and pass them to the nanodroplets, which are transported along the CNT and rotated around it.

In Fig. 13.3, we plot the translational, v , and the angular, ω_d , velocities of the nanodroplets in dependence on the wave amplitude, A . For $N_w = 1,000$, ω_d rapidly grows with A till $\omega_{d,\text{max}} \approx 50.5$ rad/ns, where the droplet is ejected from the CNT surface due to large centrifugal forces. The larger droplet rotates with $\approx 30 - 40\%$ smaller angular velocity, in analogy to the situation in a linear transport. At $A = 0.4 - 0.6$ nm, both the linear and angular velocities show certain resonant features for both droplets. At these amplitudes of the circular waves the coupling to the droplets can be dramatically altered, since the wave amplitudes are similar to the droplet sizes. Interestingly, the translational velocities, v , are very similar for both droplets. This might be due to better transfer of linear momentum to the larger droplet from circularly polarized waves.

We can perform similar analysis of the angular momentum passage from the circular wave to the droplet and back to the CNT, like we did for the linear momentum in (13.2)–(13.6). In a steady state, obtained when a circularly polarized wave of a constant amplitude is passed through the CNT, the average angular momentum of the droplet around the (equilibrium position of) CNT axis is constant. The driving momentum of force, \dot{L}_{drive} , acting on the droplet is equal to its friction counterpart, $\dot{L}_{\text{friction}}$, acting between the droplet and the CNT [45]. Assuming that

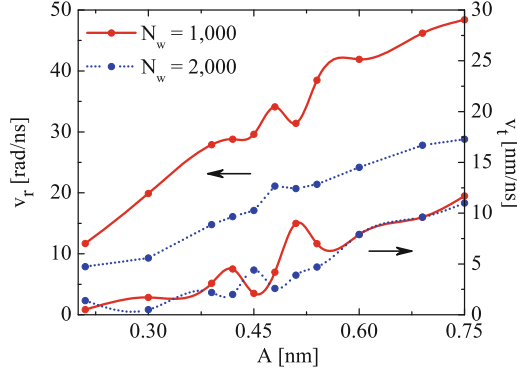


Fig. 13.3 The average translational v and angular ω_d velocities of water nanodroplets with $N_w = 1,000$ and $2,000$, in dependence on the wave amplitude, A , when driven by circularly polarized waves

the whole angular momentum density of the wave is passed to the droplet and using the approximation of the angular momentum relaxation time, we find

$$\dot{L}_{\text{drive}} = f(\mu, \omega, A) = \frac{L_{\text{droplet}}}{\tau_L} = \frac{I\omega_d}{\tau_L} = C, \quad (13.7)$$

where $f(\mu, \omega, A)$ is the angular momentum density (size) of the circularly polarized wave, I is the droplet moment of inertia with respect to the (equilibrium) CNT axis, and τ_L is the angular momentum relaxation time. In the steady state, the average rates of driving and damping are constant, as shown by C . The moment of inertia is $I = \sum_{i=1}^n m_w r_i^2 \propto N_w$, where m_w is the mass of a water molecule, and r_i is the distance of each water molecule from the (equilibrium) CNT axis. Using this I in (13.7), we find that $\omega_d \propto N_w^{-1}$, in rough agreement with Fig. 13.3.

In order to better understand the droplet-CNT dynamics, we present in Fig. 13.4 the time-dependent motion of the nanodroplet with $N_w = 1,000$ transported by circularly polarized waves. The droplet and CNT form a coupled system where the CNT vibrates around its axis and the droplet rotates around it. We describe the droplet rotation around the *actual* position of the CNT by the angle θ of the vector pointing from the center of mass of a CNT segment local to the droplet to the actual droplet center of mass. The CNT segment is defined as a 2 nm section of the CNT bisected by the droplet. The time dependence of θ for different amplitudes A is in Fig. 13.4 (top), the accompanied translation of the droplet along the CNT is in Fig. 13.4 (middle), and the radial distance of the droplet from the CNT axis is in Fig. 13.4 (bottom).

The droplet motion on the circularly polarized waves resembles *surfing*, where the droplet is sometimes grabbed better by the waves and for a while moves fast forward. At small waves, surfers cannot ride waves and neither can the droplet. This happens at $A = 0.21$ nm, where the vertical and longitudinal displacements of the

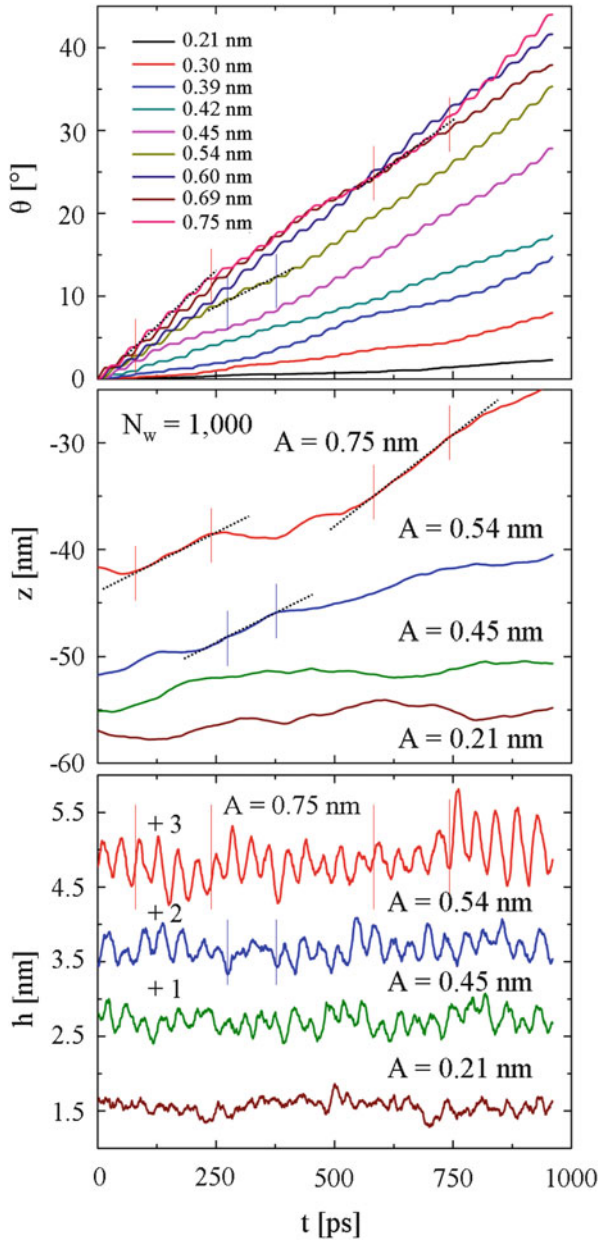


Fig. 13.4 Time-dependent angle of rotation (*top*), position (*middle*), and height (*bottom*) of the $N_w = 1,000$ droplet center of mass above the local CNT center of mass as the CNT is driven by circularly polarized waves of $\omega = 208$ GHz at amplitudes ranging from $A = 0.21$ to $A = 0.75$ nm. Tangents between vertical lines indicate regions of surfing where the nanodroplet slides down the CNT surface

droplet on the CNT are very small, as shown in Fig. 13.4 (bottom) and (middle), respectively. Therefore, a small momentum is transferred to the water droplet which almost “bobs” in place like a “buoy,” much like a surfer waiting for a wave. At larger amplitudes, the droplet can catch some of the waves and glide on them. We can see that at $A > 0.45$ nm, the droplet sometimes ($t \approx 125$ and 700 ps) starts to progress forward quickly. The same is seen even better at the larger amplitudes, $A = 0.54$ and $A = 0.75$ nm, as denoted by the dotted tangential lines. In real surfing, the gravitational force of fixed spatial orientation accelerates the surfer on the traveling tilted wave. On the CNT, the gravitational force is replaced by the inertia forces acting on the nanodroplet surfing of the circularly polarized wave.

13.3.4 Summary of Vibration-Driven Transport Simulations

We have demonstrated that TA vibrational waves on CNTs can drag nanodroplets adsorbed on their surfaces. The droplets perform translational and rotational motions, in dependence on the wave amplitude, polarization, and the droplet size. This material dragging, which complements other transport methods at the nanoscale, could be applied also on planar surfaces, such as graphene. It has potential applications in molecular delivery [46], fabrications of nanostructures [47,48], and nanofluidics [49].

13.4 Dragging of Polarizable Nanodroplets by Distantly Solvated Ions

Recent studies have demonstrated efficient dragging of molecules adsorbed on CNTs by their Coulombic scattering with electrons passing through the nanotubes [3–5]. Detection of molecular flows around CNTs by related means has also been proposed [50], tested [51–53], and applied in nanofluidic devices [54,55]. It is of a fundamental and practical interest to design techniques that could also manipulate large molecules and molecular assemblies [56,57].

13.4.1 Ion Charge Screening in Nanotubes

To follow this goal, we investigate if ions intercalated inside carbon or boron-nitride nanotubes (BNT) can be “solvated at distance” in polarizable molecular assemblies adsorbed on their surfaces [58]. In highly polar solvents, such as water, the strength and long-range order of the charge-dipole Coulombic coupling is significant even if the ion and the solvent are separated by nanometer distances. If this space is filled

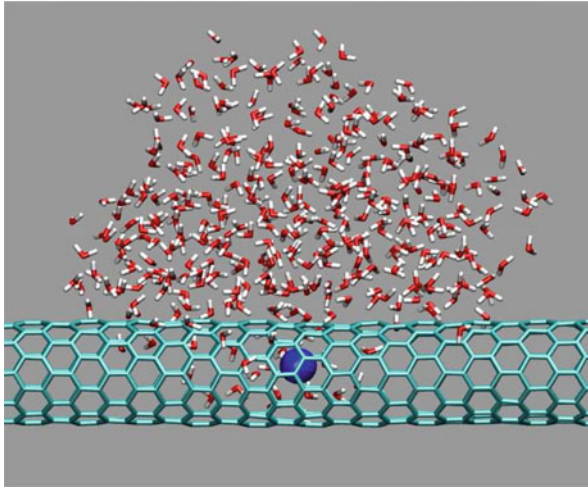


Fig. 13.5 Nanodroplet with $N_w = 400$ water molecules dragged on the surface of unpolarized (10,0) CNT by a single intercalated Na^+ cation. The ion is driven by the electric field of $\mathcal{E} = 0.1$ V/nm applied along the tube z axis

by a dielectric material with a relatively small dielectric constant, such as the wall of a nanotube with a large band gap, the coupling should be preserved at room temperatures. Therefore, polarizable nanodroplets on the nanotube surfaces might get locked to the intercalated ions and dragged by them.

We first calculate ab initio the electrostatic potential ϕ generated above a (4,3) CNT (band gap of 1.28 eV) [59] by a Li^+ ion located in its center and ϕ generated above a (5,5) BNT (band gap of 5.5 eV) [60] by a Na^+ ion. In the calculations, the 5 nm long tubes are kept neutral and frozen, since their structure is rather rigid. The potentials ϕ are obtained from NBO atomic charges, using the B3LYP density functional and the 3–21g basis set in Gaussian03 [21]. The potential ϕ of Li^+ is decreased by $\approx 25\%$ due to screening, while that of Na^+ is decreased by $\approx 10\%$. The same results are obtained in the presence of the electric field of $\mathcal{E} = 0.1$ V/nm applied along the tube axis. When the ions are shifted along the axis by a small distance d , the total energy of both systems changes by $\approx \mathcal{E}d$, as if the nanotubes are absent. These results show that the screening of the ionic field is small in selected CNTs and BNTs, where the ion can be also driven by electric fields. With this in mind, we model for simplicity the ion-droplet dynamics in some typical nanotubes and consider them to be non-polarizable.

13.4.2 Model System

In Fig. 13.5, we display a Na^+ ion intercalated inside an unpolarized (10,0) CNT that is distantly solvated in $N_w = 400$ water molecules adsorbed on the CNT surface. The system is relaxed in the box of ≈ 1000 nm³, fitting the coexistence of gas and liquid

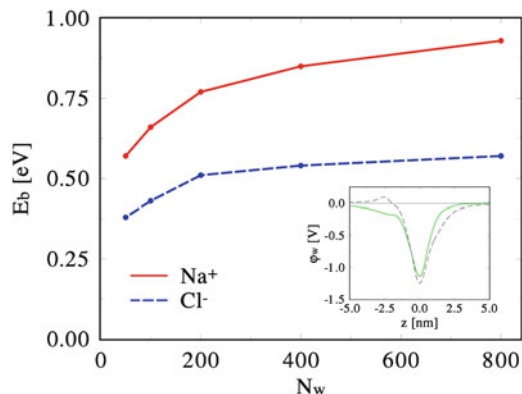


Fig. 13.6 Binding energy E_b between the Na^+ and Cl^- ions and water nanodroplets containing about N_w molecules (molecules that left to the gas phase are neglected). (*inset*) Snapshots of the electrostatic potential ϕ_w along the axis of the nanotube with the intercalated Na^+ ion

phases at the temperature of $T = 300$ K. The water droplet is spontaneously formed on the CNT even in the absence of the ion, similarly like on other fibers [61].

We model this hybrid system by molecular dynamics with the NAMD software package implementing the CHARMM27 force field as previously described. In this system we model electrostatics with the particle-mesh Ewald method [62]. We simulate the system with periodic boundary conditions in an NVT ensemble. The time step is 1 fs, and a small Langevin damping coefficient of 0.01 ps^{-1} is chosen to minimize the unphysical loss of momenta to the reservoirs [6]. The tube is aligned along the z axis, it is blocked from shifting and left free to vibrate.

13.4.3 Ion-Water Nanodroplet Coupling

We start by exploring the strength of the ion coupling to the distant solvent, characterized by the ion-droplet binding energy E_b . In Fig. 13.6, we show the obtained E_b that is averaged over 10,000 frames, separated by 500 fs intervals. For nanodroplets with $N_w = 100$ –800 waters, the binding energies E_b of the Na^+ and Cl^- ions saturate to values that are several times smaller than their solvation energies in bulk water, $E_{\text{solv}} = 7.92$ and 6.91 eV [58], respectively. For nanodroplets with $N_w < 100$, the binding energies are smaller, and at $N_w \approx 5$ –15 they become comparable to kT .

We can also estimate the coupling energy E_b analytically by assuming that the ion is located at a distance of $d \approx 0.35$ nm above a flat surface of water with the dielectric constant $\epsilon_w \approx 80$. This gives $E_b \approx -\frac{e^2}{4d} \left(\frac{\epsilon_w - 1}{\epsilon_w + 1} \right) \approx -1$ eV, in a good agreement with Fig. 13.6. The fact that in the simulations the Na^+ ion binds twice as strongly to the nanodroplet than the Cl^- ion is caused by the character of the water polarization:

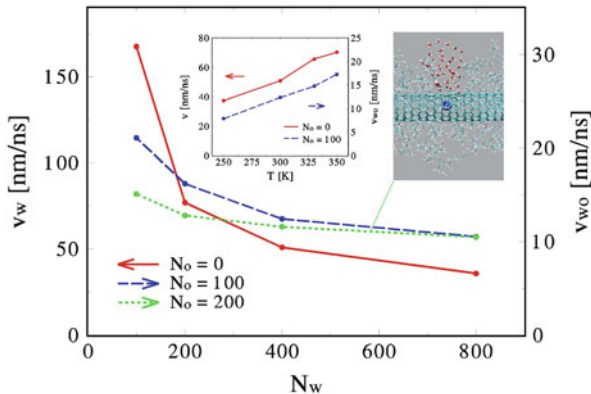


Fig. 13.7 Dependence of the nanodroplet velocity on the number of molecules N_w . Dragging of the droplet in the presence of Octane molecules is considered as well. (*right inset*) Visualization of the nanodroplet with $N_w = 50$ in $N_o = 200$ oil molecules. (*left inset*) Temperature dependence of the droplet speed for $N_w = 400$

the Na^+ ion attracts from each water the O atom that is twice more charged than the H atoms, while Cl^- attracts just one of these two H atoms. The large difference between E_b and the bulk solvation energies is caused by the fact that ions solvated in bulk water are surrounded by two to three times more water molecules that are about twice closer to them. These binding energies are proportionally decreased if the nanotube polarization is included, as discussed above.

In the inset of Fig. 13.6, we also show two snapshots of the 1D electrostatic potential generated by the water droplet ($N_w = 400$) along the axis of the nanotube with the intercalated Na^+ ion. The 1 eV deep well with a potential gradient of 0.5–1 V/nm should be large enough to block the moving ion from leaving the droplet even in the presence of electric fields of $\mathcal{E} \approx 0.1\text{--}0.2$ V/nm.

13.4.4 Nanodroplet Dragging with an Ion in an Electric Field

We continue our study by dragging the droplets with the ions in the presence of electric fields aligned along the nanotubes (see the movie [63]). The field acts on the whole system, except on the nanotube that is treated as non-polarizable. In Fig. 13.7 (left axis), we show the velocity, v_w , of droplets with N_w water molecules. The data are calculated from 50 ns simulations (≈ 50 rounds along the CNT) at $\mathcal{E}_0 = 0.1$ V/nm and $T = 300$ K. This statistical averaging is fully sufficient for the presentation of the results [6]. The obtained velocity v_w is proportional to the electric field and it strongly depends on the droplet size. It has practically the same value if the Na^+ or Cl^- ions are used for the dragging. In order to test the scalability of this dragging phenomenon, we also model a droplet with $N_w = 10,000$, located between

two parallel (10,0) CNTs separated by a 5 nm distance. If one Na^+ ion is placed in each nanotube, and both ions are driven by the field of $\mathcal{E}_0 = 0.1 \text{ V/nm}$, the droplet moves together with the ion pair at a high speed of $v_w = 6.6 \text{ nm/ns}$, due to a small contact with the CNTs.

The character of the nanodroplet motion on the nanotubes might be closer to sliding [64] than rolling [65], due to partial wetting of the CNT surface with a large van der Waals binding. In macroscopic systems, the droplet velocity for both mechanisms of motion is controlled by the momentum/energy dissipation of water layers sliding inside the droplet [64]. Both mechanisms give the qualitative dependence of the droplet velocity $v \propto e\mathcal{E}/(r\eta)$, where the droplet radius is $r \propto N_w^{1/3}$ and the water viscosity is $\eta \propto 1/T$ [66]. The results in Fig. 13.6 roughly confirm this dependence even for the motion of nanoscale droplets, but the driving speed scales more steeply with the number of water molecules, $v \propto 1/N_w^{2/3}$. In the inset, we also show for $N_w = 400$ that the temperature dependence is almost linear, $v \propto T$, as expected. To clarify more the character of motion, we test dragging of a nanodroplet by a Na^+ ion that is *directly* solvated in it. The obtained speed of the droplet is about 20% larger than when the ion is inside the tube. This is most likely caused by higher the tendency of the droplet to roll, since the dragging force acts in its center rather than on its periphery at the nanotube surface.

The character of the nanodroplet motion could be dramatically altered, if a monolayer of oil is adsorbed on the nanotube surface. In Fig. 13.7 (right axis), we show that the presence of N_o octane molecules decreases the droplet speed v_{wo} by an order of magnitude, due to friction between water and oil. Smaller droplets, $N_w < 100$, are attached to the ion by a narrow “neck” passing through the oil layer (see inset in Fig. 13.7). Larger droplets, $100 < N_w < 200$, are more or less spherical, significantly submerged inside the oil, and they share a very small surface area with the CNT. In analogy to a water droplet inside a bulk oil, their driving could be described by the Stokes law that is largely valid at the nanoscale [67, 68]. Here, it gives $F = -6\pi r\eta v_{wo}$, where $F = e\mathcal{E}_0 = 16 \text{ pN}$ is the drag force acting on the droplet, r is the droplet radius, and $\eta \approx 0.54 \text{ mPa}\cdot\text{s}$ is the viscosity of octane at $T = 300 \text{ K}$. For $N_w = 100$, we find $r \approx 3.5 \text{ \AA}$, so $v_{wo} = 4.5 \text{ m/s}$. This value is three to four times smaller than that obtained from the simulations, due to the incomplete coverage of the nanodroplet by oil.

If the nanotube is fully submerged in water instead of oil, then, on the contrary, the dynamics of the field-driven ion becomes very different [69]. We simulate this situation in a (10,0) CNT, placed in the periodic water box of $3 \times 3 \times 6.8 \text{ nm}^3$, and present in Table 13.1 the results obtained for the driving field of $\mathcal{E} = 0.1 \text{ V/nm}$. The velocities of the ions are four to five times larger than those of the ions dragging the water droplet. This is because water molecules around the submerged nanotube just rearrange fast locally when they react to the field-driven ion. At higher temperatures, the ions move faster, since their binding to the water molecules is less stable [70]. The velocities of the Cl^- ion are smaller than those of the Na^+ ion, because Cl^- easily attracts the light H atoms that are not bound (frustrated) in water molecules at the nanotube surface.

Table 13.1 Velocities of ions inside the (10,0) SWNT submerged in water and at $\mathcal{E} = 0.1$ V/nm

Ion (K)	240	270	300
Na ⁺ (m/s)	464.7	622.5	733.7
Cl ⁻ (m/s)	284.5	401.6	547.9

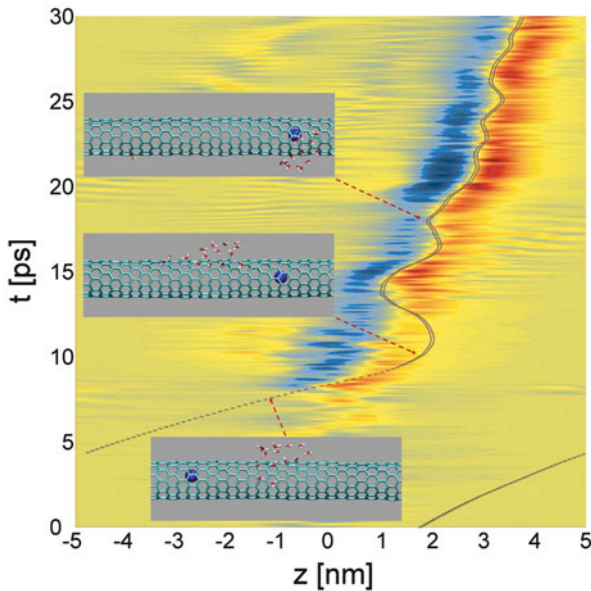


Fig. 13.8 The trajectory of the Na⁺ ion that is recaptured by a water nanodroplet with $N_w = 20$. The axial position and the time of the ion motion are shown on the *horizontal* and *vertical* axis, respectively. The electric field generated by the water molecules along the CNT axis is plotted by contours

We also discuss the *dynamical stability* of the coupled ion-droplet pair. In larger electric fields or when the nanodroplet is small, the ion might get released, and, in the model with periodic boundary conditions, it might get later recaptured by the nanodroplet. In Fig. 13.8, we plot for $\mathcal{E} = 0.02$ V/nm the trajectory of the ion that left the droplet of $N_w = 20$ and was recaptured in the next run around it. The ion's trajectory is shown by the dark line, and the time-frame separation on the vertical axis is 100 fs. The electric field along the CNT axis created by the ion-polarized droplet is plotted by contours. The positive/negative regions that lock the ion are obtained from the derivative taken at the sides of the potential well (see inset of Fig. 13.6).

The ion released from the droplet goes once around the tube and reapproaches the droplet with the velocity of $v_{ini} \approx 1,400$ m/s (bottom). After it gets closer to the droplet, the water molecules become fast polarized (inset at $z = -1.3$ nm, $t = 7$ ps). The ion first passes around the droplet, just to be attracted back by several chained

molecules protruding from the droplet ($z = 1.7$ nm, $t = 10.0$ ps). This is possible, since a chain of five hydrogen-bonded and aligned water molecules generate at the distance of 1 nm the field of ≈ 0.17 V/nm, which is opposite to and almost an order of magnitude larger than the external field. The deceleration of the ion by this large induced field causes the coupled system to gain high Coulombic potential energy. Thus the ion position oscillates three to four times, before it is fully seized back by the droplet ($z = 2$ nm, $t = 18$ ps). The two start to move together at a much smaller velocity $v_{\text{end}} \approx 130$ m/s, while the waters are already interconnected. If the droplet does not catch the ion within several of its runs around the periodic system, the ion might heat and temporally evaporate the droplet. The transient oscillations observed in this ion catching closely resemble quasi-particle formation in condensed matter systems [71].

13.4.5 Summary of Nanodroplet Dragging by Distantly Solvated Ions

The Coulombic dragging of molecules on the surfaces of nanotubes by ions and ionic solutions flowing through them complements the passive transport of gases [72, 73] and liquids [74–77] through CNTs. These phenomena might be used in molecular delivery, separation, desalination, and manipulation of nanoparticles at the nanoscale. When integrated into modern lab-on-a-chip techniques, the methodology could lead to a number of important nanofluidic applications [46].

13.5 Nanodroplet Activated and Guided Folding of Graphene Nanostructures

Recently, graphene monolayers have been prepared and intensively studied [78–81]. Graphene nanoribbons have also been synthesized [82–84], and etched by using lithography [85, 86] and catalytic [87, 88] methods. *Graphene flakes* with strong interlayer vdW binding can self-assemble into larger structures [89–91]. Individual flakes with high elasticity [92–94] could also fold into a variety of 3D structures, such as carbon nanoscrolls [95, 96]. These nanoscrolls could be even prepared from single graphene sheets, when assisted by certain gases or alcohols [97, 98]. In order to reproducibly prepare such stable or metastable structures of different complexity, (1) the potential barriers associated with graphene deformation need to be overcome, (2) the folding processes should be guided, and (3) the final structures need to be well coordinated and stabilized by vdW or other coupling mechanisms.

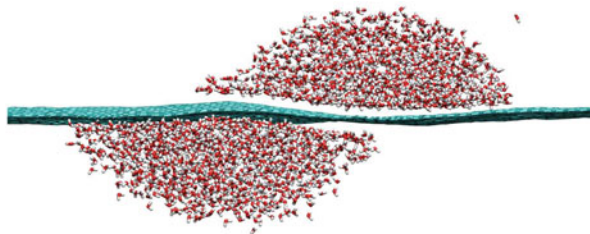


Fig. 13.9 Side view on two water nanodroplets, each with $N_w = 1300$ molecules, adsorbed on the opposite sides of a graphene sheet. The nanodroplets create two shallow holes in the graphene. Eventually, the nanodroplets become adjacent but stay highly mobile. Their dynamical coupling is realized by the minimization of the graphene bending energy associated with the two holes

13.5.1 Nanodroplet Coupling to Graphene

Carbon nanotubes can serve as a railroad for small water droplets [16]. CNTs submerged in water can assemble into micro-rings around bubbles formed by ultrasonic waves [99]. Similar assembly effects might work in 2D graphene-based systems. For example, liquid droplets can induce wrinkles on thin polymer films by strong capillary forces [100]. Droplets can also guide folding of 3D microstructures from polymer (PDMS) sheets [101]. *The question is if nanodroplets (ND) can activate and guide folding of graphene flakes of complex shapes, analogously like chaperones fold proteins* [102].

To answer this question, we study first the interaction of a water nanodroplet, of $N_w = 1,300$ waters, with a graphene sheet, of the size of $15 \times 12 \text{ nm}^2$. It turns out that the nanodroplet, equilibrated at $T = 300 \text{ K}$, induces a shallow hole in the graphene sheet, with the curvature radius of $R \approx 5 \text{ nm}$.¹ The hole formation is driven by vdW coupling, which tends to minimize the surface of the naked droplet but maximize the surface of the graphene-dressed droplet. As shown in Fig. 13.9, two such droplets adsorbed on the opposite sides of the graphene sheet couple to save on the hole formation energy. The two droplets stay together during a correlated diffusion motion on the graphene surface.

¹In the MD simulations, we apply the Langevin dynamics with 0.01 ps^{-1} damping coefficient, to minimize the unphysical loss of momentum [16], and the time step is 1 fs. The systems are simulated as NVT ensembles inside periodic cells of the following sizes: Fig. 13.9 ($55 \times 35 \times 35 \text{ nm}^3$), Fig. 13.10 (up) ($30 \times 35 \times 35 \text{ nm}^3$), Fig. 13.10 (bottom) ($30 \times 35 \times 35 \text{ nm}^3$), Fig. 13.11 ($15 \times 85 \times 25 \text{ nm}^3$), Fig. 13.12 ($20 \times 120 \times 20 \text{ nm}^3$), and Fig. 13.14 ($20 \times 75 \times 20 \text{ nm}^3$). The graphene–water (or graphene–graphene) binding energies are calculated as the difference of the total vdW energy of the system, when the system components are at the normal binding distance, and when they are separated by 5 nm. Averaging of the energies is done over 100 consecutive frames of the simulation trajectory, with a 1 ps time interval.

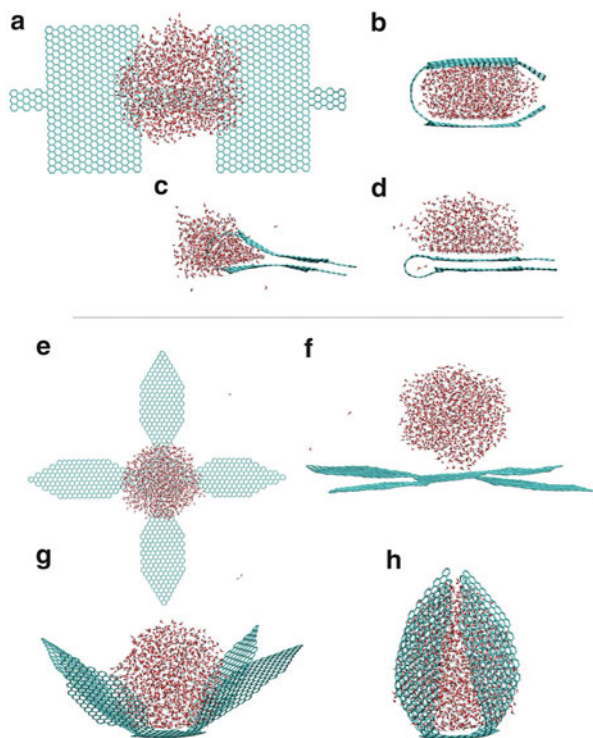


Fig. 13.10 (a)–(d) Water nanodroplet activated and guided folding of two graphene flakes connected by a narrow bridge. The nanodroplet is squeezed away when the system is heated to $T = 400$ K. (e)–(h) Nanodroplet assisted folding of a star-shaped graphene flake, resembling the action of a “meat-eating flower”

13.5.2 Folding of Flakes

Intrigued by the action of NDs on graphene, we test if they can activate and guide folding of graphene flakes of various shapes. As shown in Fig. 13.10a, we first design a graphene nanoribbon, where two rectangular 3×5 nm² flakes are connected by a narrow stripe of 2.5×0.73 nm². In the simulations, we fix a few stripes of benzene rings on the right flake, which could be realized if the graphene is partly fixed at some substrate, and position a water nanodroplet ($N_w = 1,300$) above the center of the two flakes ($T = 300$ K). Figure 13.10b after $t \approx 250$ ps, both flakes bind with the droplet and bend the connecting bridge to form a metastable sandwich structure. Figure 13.10c when the temperature is raised to $T = 400$ K, the droplet becomes more mobile and fluctuating. Within $t \approx 50$ ps, the two flakes start to bind each other, and the water droplet is squeezed away. Figure 13.10d after another $t \approx 60$ ps, the flakes join each other into a double layer, and the droplet stays on the top of one flake. When a smaller water droplet with $N_w = 800$ is placed on the nanoribbon, it induces its folding in a similar way and becomes squeezed out even faster in Fig. 13.10c, d.

Similarly, we study the folding of a star-shaped graphene nanoribbon with four blades connected to a central flake, as shown in Fig. 13.10e–f. At $T = 300$ K, a water droplet ($N_w = 1,300$) is initially positioned at the height of $h \approx 0.5$ nm above the central flake. Figure 13.10g the droplet binds by vdW coupling with the central flake and induces bending of the four blades. Figure 13.10h after $t \approx 1$ ns, the four blades fold into a closed structure, with waters filling its interior. This effect resembles the action of a “meat-eating flower” [103], where the graphene capsule can store and protect the liquid content in various environments. Notice that slight asymmetry of the flake does not change the character of the assembly process. In real systems, other molecules might also be adsorbed on the graphene flakes. Although these molecules are not considered here, they might coalesce with the water droplets and modify their properties in the assembly process. Experimentally, the droplets could be deposited by Dip-Pen nanolithography [104] or AFM [105]. This deposition can also cause side effects not considered here, such as passage additional momentum to the folding sheet.

Folding of the two flakes into the sandwich, shown in Fig. 13.10a, b, is driven by the decrease of the water–graphene binding energy, $E_{g-w} = -\sigma_{g-w}A_{g-w}$. Here, we estimate the density of the binding energy from our MD simulations (see Footnote 1) to be $\sigma_{g-w} \approx 20.8$ kcal/(mol nm²). The water–graphene binding area of the narrow stripe (initial area) and the two flakes (final area) are $A_{g-w}^{\text{ini}} = 2.5 \times 0.7 = 1.75$ nm² and $A_{g-w}^{\text{end}} = 3 \times 5 \times (2) = 30$ nm², respectively. The elastic bending energy of the connecting stripe is $E_{\text{ela}} = \sigma_{\text{ela}}A_{\text{ela}}$, where $A_{\text{ela}} \approx A_{g-w}^{\text{ini}}$ is the bending area, and $\sigma_{\text{ela}} = \frac{1}{2}D\kappa^2$ is calculated for $D = 27.9$ kcal/mol and $\kappa = 1/R_g$, where R_g is the graphene ribbon radius. In this case, $R_g \approx 1$ nm, so $\sigma_{g-w} > \sigma_{\text{ela}} \approx 14$ kcal/(mol nm²). This, together with $A_{g-w} \approx A_{\text{ela}}$, valid at the beginning of the folding process, means that $E_{g-w} + E_{\text{ela}} < 0$. During the folding process, the sandwich configuration becomes further stabilized, since E_{g-w} decreases by an order of magnitude, due to $A_{g-w} = A_{g-w}^{\text{end}}$.

The final squeezing of the nanodroplet out of the sandwich, shown in Fig. 13.10c, d, means that graphene–graphene vdW binding is preferable to graphene–water vdW binding, for the force field parameters used in CHARMM27.

13.5.3 Folding of Ribbons

We now test if NDs can induce folding of graphene nanoribbons. As shown in Fig. 13.11a, we use a 30×2 nm² graphene nanoribbon, with one end fixed. At $T = 300$ K, a ND with $N_w = 1,300$ waters is positioned above the free end of the ribbon. Figure 13.11b the free end starts to fold fast around the droplet. Figure 13.11c after $t = 0.6$ ns, the free end folds into a knot structure, touches the ribbon surface and starts to slide fast on it, due to strong vdW binding. Figure 13.11d while the knot is sliding on the ribbon, the droplet is deformed into a droplet-like shape that slips and rolls inside the knot [16]. After sliding over $l = 20$ nm, the water filled knot gains

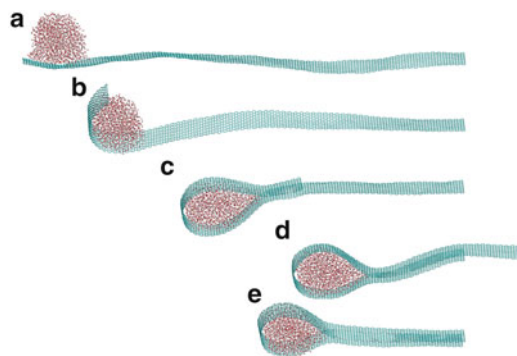


Fig. 13.11 Folding and sliding of a graphene ribbon with the size of 30×2 nm, which is activated and guided by a nanodroplet with $N_w = 1,300$ waters and the radius of $R_d \approx 2.1$ nm. (a)–(c) The free ribbon end folds around the droplet into a knot structure that slides on the ribbon surface (d) and (e)

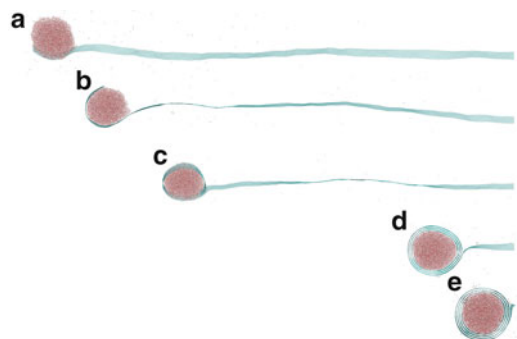


Fig. 13.12 Folding and rolling of a graphene ribbon with the size of 90×2 nm, which is activated and guided by a nanodroplet with $N_w = 10,000$ waters and the radius of $R_d \approx 4.2$ nm. (a) and (b) The ribbon tip folds around the water droplet into a wrapped cylinder, and (c)–(e) the wrapped cylinder is induced to roll on the ribbon surface (c)–(e)

the velocity of $v_w \approx 100$ m/s. This velocity is controlled by the rate of releasing potential energy, due to binding but reduced by bending, into the kinetic degrees of freedom, damped by friction. Figure 13.11d the sliding ribbon reaches the fixed end and overstretches into the space, due to its large momentum. Figure 13.11e it oscillates back and forth two to three times before the translational kinetic energy is dissipated.

The existence of CNTs raises the question if we could also “roll” graphene ribbons. This might happen when the droplet is larger and thus when it controls more the ribbon dynamics. In Fig. 13.12a, we simulate the folding of a 90×2 nm² graphene ribbon (one end is fixed) at $T = 300$ K, when a droplet of $N_w = 10,000$ is initially positioned above the tip of the ribbon. Figure 13.12b, c as before, within $t = 2$ ps, the ribbon tip folds around the spherical droplet into a closed circular

cylinder. Figure 13.12d this time, the approaching free end touches the surface at a larger angle and forms a cylinder around the droplet that starts to roll fast on the ribbon surface, like a contracting tongue of a chameleon. After rolling over $l = 60$ nm, the translational and rolling velocities are $v_t \approx 50$ m/s and $\omega_r \approx 12$ rad/ns, respectively. Figure 13.12e the cylinder rolls until the fixed end of the ribbon, where the rolling kinetic energy is eventually dissipated. The folded ribbon forms a multilayered ring structure, similar to multiwall nanotube, which is filled by water.

Let us analyze the conditions under which a graphene ribbon folds. Analogously to the folding of flakes, shown in Fig. 13.10, the folding of ribbon is driven by the competition between the graphene–water binding energy, $E_{g-w} = -\sigma_{g-w}A_{g-w}$, and the graphene bending energy, $E_{ela} = \sigma_{ela}A_{ela}$. From the energy condition, $E_{g-w} + E_{ela} < 0$, we obtain

$$\frac{A_{g-w}}{A_{ela}} > \frac{\sigma_{ela}}{\sigma_{g-w}}. \quad (13.8)$$

In Fig. 13.11, the water droplet has the radius $R_d \approx 2.1$ nm. Assuming that $R_g \approx R_d$, we obtain from the above formula for σ_{ela} that $\sigma_{ela} = 3.2$ kcal/(mol nm²) and $\sigma_{ela}/\sigma_{g-w} \approx 0.15$. Since, $A_{g-w}/A_{ela} \approx 1$, we see that this case easily fulfills the condition in (13.8). The graphene ribbon slides on itself, and this situation can be called the “sliding phase”.

The ratio A_{g-w}/A_{ela} and indirectly also σ_{ela} depend on the ratio of the ribbon width w to the droplet radius R_d , which thus controls the character of the folding process. When $w < 2R_d$, the droplet can bind, in principle, on the whole width of the ribbon, so $A_{g-w} \approx A_{ela}$. For even larger droplets, we eventually get $w < 0.5R_d$, where our simulations show that the ribbon binds fully to the droplet surface. In this limit, we observe that after folding once around the droplet circumference the ribbon approaches itself practically at the wetting angle, and gains the dynamics characteristic for the “rolling phase”, shown in Fig. 13.12.

When $w > 2R_d$, it becomes very difficult for the small droplet to induce folding of the wide ribbon. Then, the droplet binds to the ribbon at an approximately circular area, with a radius $\approx R_d$, because the water contact angle on graphene is about 90° and the droplet has almost the shape of a half-sphere [106]. If we assume that $R_g \approx R_d$, we have $A_{g-w} \approx \pi R_d^2$ and $A_{ela} \approx 2R_d w$. From (13.8) and $\sigma_{ela} = \frac{1}{2} D \kappa^2 = \frac{1}{2} D \frac{1}{R_d^2}$, we then obtain the condition for the ribbon folding

$$R_d^3 > \frac{Dw}{\pi \sigma_{g-w}}. \quad (13.9)$$

On the other hand, this means that the ribbon does not fold when $w \geq CR_d^3$ ($C = \pi \sigma_{g-w}/D \approx 4$ nm⁻²), and this situation can be called the “nonfolding phase”.

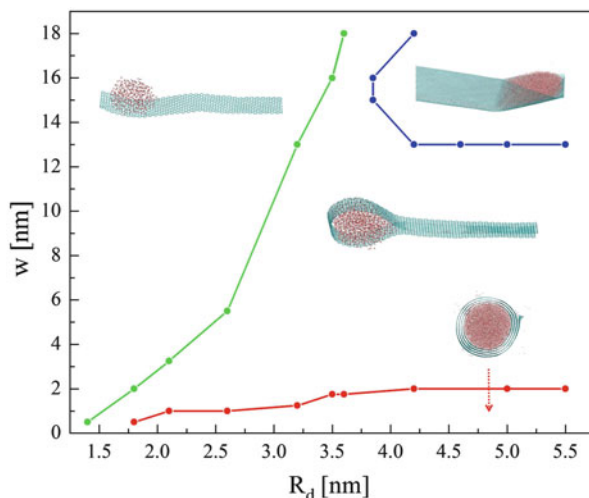


Fig. 13.13 The phase diagram of a nanodroplet and graphene nanoribbon with different folding dynamics. We display the nonfolding, sliding, rolling, and zipping phases

13.5.4 Nanodroplet-Graphene Phase Diagram

In Fig. 13.13, we summarize the results of our simulations in a phase diagram. We display four “phases” characterizing the ribbon dynamics, separated by phase boundary lines. They are called nonfolding, sliding, rolling, and zipping, where the first three were described and briefly analyzed above. The nonfolding phase, where the ribbon end does not fold around the droplet, is characterized by the cubic boundary derived above and shown in Fig. 13.13 (left). In the simulations, we obtain the value $C \approx 2.8 \text{ nm}^{-2}$, in close agreement with the above prediction. The nonfolding phase is adjacent with the sliding phase, which is separated from the rolling phase by the boundary line $w \approx \frac{1}{2} R_d$.

When the graphene ribbon becomes several times wider than the droplet diameter, it may fold around it in the orthogonal direction. Then, the folding dynamics of the graphene ribbon has a character of zipping. This situation corresponds to the “zipping phase”, shown in the right top corner of the phase diagram in Fig. 13.13 and explained in detail in Fig. 13.14. Figure 13.14a we place a droplet of $N_w = 17,000$ at the free end of the ribbon of the size of $60 \times 16 \text{ nm}^2$. Figure 13.14b the ribbon folds from the two sides of the droplet within $t \approx 250 \text{ ps}$. Figure 13.14c at $t \approx 450 \text{ ps}$, the ribbon starts to “zip,” where its two sides touch each other. Figure 13.14d the zipping process continues, and the droplet is transported along the ribbon. After zipping over $l \approx 40 \text{ nm}$, the droplet gains a translational velocity of $v_t \approx 63 \text{ m/s}$. In the zipped region, a chain of water molecules resides inside the turning line of the zipped ribbon. This region can be used like an artificial channel, similarly like CNTs.

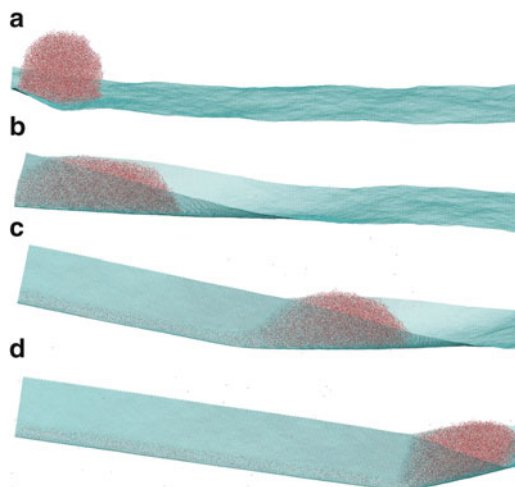


Fig. 13.14 Folding and zipping of a graphene ribbon with the size of 60×16 nm, which is activated and guided by a nanodroplet with $N_w = 17,000$ waters and the radius of $R_d \approx 5$ nm. (a) and (b) The ribbon end folds around the droplet. (c) and (d) The zipping propagates along the ribbon until the fixed end, while water channel is formed in the graphene sleeve

13.6 Conclusions

In summary, we have demonstrated that water nanodroplets can activate and guide folding of graphene nanostructures. The folding can be realized by different types of motions, such as bending, sliding, rolling, or zipping that lead to stable or metastable structures, such as sandwiches, capsules, knots, and rings. These structures can be the building blocks of functional nanodevices, with unique mechanical, electrical, or optical properties [47]. We have also shown how water nanodroplets could be used to carry materials on graphitic nanocarbon supports. We explored drag phenomena of nanodroplets on CNTs by vibrations and by coupling to distantly solvated ions. These studies can lead to future applications in molecular delivery, fabrications of nanostructures, and nanofluidics.

References

1. Iijima, S.: Helical microtubules of graphitic carbon. *Nature* **354**, 56–58 (1991)
2. Saito, R., Dresselhaus, G., Dresselhaus, M.S.: *Physical Properties of Carbon Nanotubes*. World Scientific, London (1998)
3. Král, P., Tománek, D.: Laser-driven atomic pump. *Phys. Rev. Lett.* **83**, 5373–5376 (1999)
4. Regan, B.C., Aloni, S., Ritchie, R.O., Dahmen, U., Zettl, A.: Carbon nanotubes as nanoscale mass conveyors. *Nature* **428**, 924–927 (2004)

5. Svensson, K., Olin, H., Olsson, E.: Nanopipettes for metal transport. *Phys. Rev. Lett.* **93**, 145901 (2004)
6. Wang, B., Král, P.: Coulombic dragging of molecules on surfaces induced by separately flowing liquids. *J. Am. Chem. Soc.* **128**, 15984 (2006)
7. Wang, B., Král, P.: Dragging of polarizable nanodroplets by distantly solvated ions. *Phys. Rev. Lett.* **101**, 046103 (2008)
8. Zhao, Y.C., Song, L., Deng, K., Liu, Z., Zhang, Z.X., Yang, Y.L., Wang, C., Yang, H.F., Jin, A.Z., Luo, Q., Gu, C.Z., Xie, S.S., Sun, L.F.: Individual water-filled single-walled carbon nanotubes as hydroelectric power converters. *Adv. Mater.* **20**, 1772–1776 (2008)
9. Schoen, P.A.E., Walther, J.H., Arcidiacono, S., Poulidakos, D., Koumoutsakos, P.: Nanoparticle traffic on helical tracks: thermophoretic mass transport through carbon nanotubes. *Nano Lett.* **6**, 1910–1917 (2006)
10. Barreiro, A., Ruráli, R., Hernandez, E.R., Moser, J., Pichler, T., Forro, L., Bachtold, A.: Subnanometer motion of cargoes driven by thermal gradients along carbon nanotubes. *Science* **320**, 775–778 (2008)
11. Zambrano, H.A., Walther, J.H., Koumoutsakos, P., Sbalzarini, I.F.: Thermophoretic motion of water nanodroplets confined inside carbon nanotubes. *Nano Lett.* **9**, 66–71 (2006)
12. Shiomi, J., Maruyama, S.: Water transport inside a single-walled carbon nanotube driven by a temperature gradient. *Nanotechnology* **20**, 055708 (2009)
13. Insepov, Z., Wolf, D., Hassanein, A.: Nanopumping using carbon nanotubes. *Nano Lett.* **6**, 1893–1895 (2006)
14. Wang, Q.: Atomic transportation via carbon nanotubes. *Nano Lett.* **9**, 245–249 (2009)
15. Russell, J.T., Wang, B., Král, P.: Nanodroplet transport on vibrated nanotubes. *Phys. Chem. Lett.* **3**, 313–357 (2012)
16. Wang, B., Král, P.: Dragging of polarizable nanodroplets by distantly solvated ions. *Phys. Rev. Lett.* **101**, 046103 (2008)
17. Patra, N., Wang, B., Král, P.: Nanodroplet activated and guided folding of graphene nanostructures. *Nano Lett.* **9**, 3766–3771 (2009)
18. Phillips, J.C., Braun, R., Wang, W., Gumbart, J., Tajkhorshid, E., Villa, E., Chipot, C., Skeel, R.D., Kale, L., Schulten, K.: Scalable molecular dynamics with NAMD. *J. Comput. Chem.* **26**, 1781–1802 (2005)
19. MacKerell, A.D. Jr., Bashford, D., Bellot, M., Dunbrack, R.L., Evanseck, J.D., Field, M.J., Fischer, S., Gao, J., Guo, H., Ha, S., Joseph-McCarthy, D., Kuchnir, L., Kuczera, K., Lau, F.T.K., Mattos, C., Michnick, S., Ngo, T., Nguyen, D.T., Prodhom, B., Reiher, W.E. III, Roux, B., Schlenkrich, M., Smith, J.C., Stote, R., Straub, J., Watanabe, M., Wiorkiewicz-Kuczera, J., Yin, D., Karplus, M.: All-atom empirical potential for molecular modeling and dynamics studies of proteins. *J. Phys. Chem. B* **102**, 3586–3617 (1998)
20. Humphrey, W., Dalke, A., Schulten, K.: VMD: visual molecular dynamics. *J. Mol. Graph.* **14**, 33–38 (1996)
21. Frisch, M.J., et al: Gaussian 03, Revision C.02. Gaussian, Wallingford (2004)
22. Vukovic, L., Král, P.: Coulombically driven rolling of nanorods on water *Phys. Rev. Lett.* **103**, 246103 (2009)
23. Tersoff, J.: Energies of fullerenes. *J. Phys. Rev. B* **46**, 15546–15549 (1992)
24. Kudin, K.N., Scuseria, E.G.: C₂F, BN, and C nanoshell elasticity from ab initio computations. *Phys. Rev. B* **64**, 235406–234515 (2001)
25. Arroyo, M., Belytschko, T.: Finite crystal elasticity of carbon nanotubes based on the exponential Cauchy-Born rule. *Phys. Rev. B* **69**, 115415–115425 (2004)
26. Lu, Q., Arroyo, M., Huang, R.: Elastic bending modulus of monolayer graphene. *J. Phys. D Appl. Phys.* **42**, 102002–102007 (2009)
27. Wang, Z., Zhe, J.: Recent advances in particle and droplet manipulation for lab-on-a-chip devices based on surface acoustic waves. *Lab Chip* **11**, 1280–1285 (2011)
28. Hashimoto, H., Koike, Y., Ueha, S.: Transporting objects without contact using flexural travelling waves. *J. Acoust. Soc. Am.* **103**, 3230–3233 (1998)

29. Kim, G.H., Park, J.W., Jeong, S.H.: Analysis of dynamic characteristics for vibration of flexural beam in ultrasonic transport system. *J. Mech. Sci. Technol.* **23**, 1428–1434 (2009)
30. Miranda, E.C., Thomsen, J.J.: Vibration induced sliding: theory and experiment for a beam with a spring-loaded mass. *Nonlinear Dyn.* **19**, 167–186 (1998)
31. Vielsack, P., Spiess, H.: Sliding of a mass on an inclined driven plane with randomly varying coefficient of friction. *J. Appl. Mech.* **67**, 112–116 (2000)
32. Long, Y.G., Nagaya, K., Niwa, H.: Vibration conveyance in spatial-curved tubes. *J. Vib. Acoust.* **116**, 38–46 (1994)
33. Biwersi, S., Manceau, J.-F., Bastien, F.: Displacement of droplets and deformation of thin liquid layers using flexural vibrations of structures. influence of acoustic radiation pressure. *J. Acoust. Soc. Am.* **107**, 661–664 (2000)
34. Wixforth, A., Strobl, C., Gauer, C., Toegl, A., Scriba, J., Guttenberg, Z.V.: Acoustic manipulation of small droplets. *Anal. Bioanal. Chem.* **379**, 982–991 (2004)
35. Alzuaga, S., Manceau, J.-F., Bastien, F.: Motion of droplets on solid surface using acoustic radiation pressure. *J. Sound Vib.* **282**, 151–162 (2005)
36. Bennes, J., Alzuaga, S., Chabe, P., Morain, G., Cheroux, F., Manceau, J.-F., Bastien, F.: Action of low frequency vibration on liquid droplets and particles. *Ultrasonics* **44**, 497–502 (2004)
37. Jiao, Z.J., Huang, X.Y., Nguyen, N.-T.: Scattering and attenuation of surface acoustic waves in droplet actuation. *J. Phys. A Math. Theor.* **41**, 355502 (2008)
38. Mele, E.J., Král, P.: Electric polarization of heteropolar nanotubes as a geometric phase. *Phys. Rev. Lett.* **88**, 056803 (2002)
39. Michalski, P.J., Sai, N.A., Mele, E.J.: Continuum theory for nanotube piezoelectricity. *Phys. Rev. Lett.* **95**, 116803 (2005)
40. Král, P., Thanopoulos, I., Shapiro, M.: Coherently controlled adiabatic passage. *Rev. Mod. Phys.* **79**, 53–77 (2007)
41. Schneider, T., Stoll, E.: Molecular-dynamics study of three-dimensions one-component model for distortive phase transitions. *Phys. Rev. B* **17**, 1302–1322 (1978)
42. Matsumoto, M., Kunisawa, T., Xiao, P.: Relaxation of phonons in classical MD simulation. *J. Therm. Sci. Technol.* **3**, 159–166 (2008)
43. Král, P.: Linearized quantum transport equations: AC conductance of a quantum wire with an electron-phonon interaction. *Phys. Rev. B* **53**, 11034–11050 (1996)
44. Benumof, R.: Momentum propagation by traveling waves on a string. *Am. J. Phys.* **50**, 20–25 (1982)
45. Segal, D., Král, P., Shapiro, M.: Ultraslow phonon-assisted collapse of tubular image states. *Surf. Sci.* **577**, 86–92 (2005)
46. Craighead, H.G.: Future lab-on-a-chip technologies for interrogating individual molecules. *Nature* **442**, 387–393 (2006)
47. Baughman, R.H., Cui, C.X., Zakhidov, A.A., Iqbal, Z., Barisci, J.N., Spinks, G.M., Wallace, G.G., Mazzoldi, A., De Rossi, D., Rinzler, A.G., Jaschinski, O., Roth, S., Kertesz, M.: Carbon nanotube actuators. *Science* **284**, 1340–1344 (1999)
48. Spinks, G.M., Wallace, G.G., Fifield, L.S., Dalton, L.R., Mazzoldi, A., De Rossi, D., Khayrullin, I.I., Baughman, R.H., Pneumatic carbon nanotube actuators. *Adv. Mater.* **14**, 1728–1732 (2002)
49. Schoch, R.B., Han, J.Y., Renaud, P., Transport phenomena in nanofluidics. *Rev. Mod. Phys.* **80**, 839–883 (2008)
50. Král, P., Shapiro, M.: Nanotube electron drag in flowing liquids. *Phys. Rev. Lett.* **86**, 131 (2001)
51. Ghosh, S., Sood, A.K., Kumar, N.: Carbon nanotube flow sensors. *Science* **299**, 1042 (2003). US Patent No. 6718834 B1
52. Sood, A.K., Ghosh, S.: Direct generation of a voltage and current by gas flow over carbon nanotubes and semiconductors. *Phys. Rev. Lett.* **93**, 086601 (2004)
53. Subramaniam, C., Pradeep, T., Chakrabarti, J.: Flow-induced transverse electrical potential across an assembly of gold nanoparticles. *Phys. Rev. Lett.* **95**, 164501 (2005)
54. Bournon, B., Wong, J., Miko, C., Forro, L., Bockrath, M.: A nanoscale probe for fluidic and ionic transport. *Nat. Nanotech.* **2**, 104 (2006)

55. Fu, J.P., Schoch, R.B., Stevens, A.L., Tannenbaum, S.R., Han, J.Y.: A patterned anisotropic nanofluidic sieving structure for continuous-flow separation of DNA and proteins. *Nat. Nanotech.* **2**, 121 (2007)
56. Linke, H., et al.: Self-propelled Leidenfrost droplets. *Phys. Rev. Lett.* **96**, 154502 (2006)
57. Akin, D., et al.: Bacteria-mediated delivery of nanoparticles and cargo into cells. *Nat. Nanotech.* **2**, 441–449 (2007)
58. Hitoshi, O., Radnai, T.: Structure and dynamics of hydrated ions. *Chem. Rev.* **93**, 1157 (1993)
59. Cabria, I., Mintmire, J.W., White, C.T.: Metallic and semiconducting narrow carbon nanotubes. *Phys. Rev. B* **67**, 121406(R) (2003)
60. Blasé, X., Rubio, A., Louie, S.G., Cohen, M.L.: Stability and band gap constancy of boron nitride nanotubes. *Europhys. Lett.* **28**, 335 (1994)
61. McHale, G., Newton, M.I., Carroll, B.J.: The shape and stability of small liquid drops on fibers. *Oil Gas Sci. Technol. Rev. IFP* **56**, 47 (2006)
62. Darden, T., York, D., Pedersen, L.: Particle mesh Ewald: An Nlog(N) method for Ewald sums in large systems. *J. Chem. Phys.* **98**, 10089 (1993)
63. See EPAPS Document No. E-PRLTAO-101-06380 for three movies. For more information on EPAPS, (2008) see <http://www.aip.org/pubservs/epaps.html>
64. Kim, H.Y., Lee, H.J., Kang, B.H.: Sliding of liquid drops down an inclined solid surface. *J. Coll. Int. Sci.* **247**, 372 (2002)
65. Mahadevan, L., Pomeau, Y.: Rolling droplets. *Phys. Fluids* **11**, 2449 (1999)
66. Brancker, A.V.: Viscosity-temperature dependence. *Nature* **166**, 905 (1950)
67. Vergeles, M., Keblinski, P., Koplik, J., Banavar, J.R.: Stokes drag and lubrication flows: a molecular dynamics study. *Phys. Rev. E* **53**, 4852 (1996)
68. Squires, T.M., Quake, S.R.: Microfluidics: fluid physics at the nanoliter scale. *Rev. Mod. Phys.* **77**, 977 (2005)
69. Mills, D.L.: Image force on a moving charge. *Phys. Rev. B* **15**, 763 (1977)
70. Laage, D., Hynes, J.T.: A molecular jump mechanism of water reorientation. *Science* **311**, 832 (2006)
71. Král, P., Jauho, A.P.: Resonant tunneling in a pulsed phonon field. *Phys. Rev. B* **59**, 7656 (1999)
72. Skoulidas, A.I., Ackerman, D.M., Johnson, J.K., Sholl, D.S.: Rapid transport of gases in carbon nanotubes. *Phys. Rev. Lett.* **89**, 185901 (2002)
73. Holt, J.K., et al.: Fast mass transport through sub-2-nanometer carbon nanotubes. *Science* **312**, 1034 (2006)
74. Majumder, M., Chopra, N., Andrews, R., Hinds, B.J.: Nanoscale hydrodynamics: enhanced flow in carbon nanotubes. *Nature* **483**, 44 (2005)
75. Wang, Z., Ci, L., Chen, L., Nayak, S., Ajayan, P.M., Koratkar, N.: Polarity-dependent electrochemically controlled transport of water through carbon nanotube membranes. *Nano Lett.* **7**, 697 (2007)
76. Zhou, J.J., Noca, F., Gharib, M.: Flow conveying and diagnosis with carbon nanotube arrays. *Nanotechnology* **17**, 4845 (2006)
77. Whitby, M., Quirke, N.: Fluid flow in carbon nanotubes and nanopipes. *Nat. Nanotechnol.* **2**, 87 (2007)
78. Novoselov, K.S., Geim, A.K., Morozov, S.V., Jiang, D., Zhang, Y., Dubonos, S.V., Grigorieva, I.V., Firsov, A.A.: Electric field effect in atomically thin carbon films. *Science* **306**, 666–669 (2004)
79. Geim, A.K., Novoselov, K.S.: The rise of graphene. *Nat. Mater.* **6**, 183–191 (2007)
80. Berner, S., Corso, M., Widmer, R., Groening, O., Laskowski, R., Blaha, P., Schwarz, K., Goriachko, A., Over, H., Gsell, S., Schreck, M., Sachdev, H., Greber, T., Osterwalder, J.: Boron nitride nanomesh: functionality from a corrugated monolayer. *Angew. Chem. Int. Ed.* **46**, 5115–5119 (2007)
81. Laskowski, R., Blaha, P., Gallauner, T., Schwarz, K.: Single-layer model of the hexagonal boron nitride nanomesh on the Rh(111) surface. *Phys. Rev. Lett.* **98**, 106802 (2007)

82. Li, X., Wang, X., Zhang, L., Lee, S., Dai, H.: Chemically derived, ultrasmooth graphene nanoribbon semiconductors. *Science* **319**, 1229–1232 (2008)
83. Jiao, L., Zhang, L., Wang, X., Diankov, G., Dai, H.: Narrow graphene nanoribbons from carbon nanotubes. *Nature* **458**, 877–880 (2009)
84. Kosynkin, D.V., Higginbotham, A.L., Sinitskii, A., Lomeda, J.R., Dimiev, A., Price, B.K., Tour, J.M.: Longitudinal unzipping of carbon nanotubes to form graphene nanoribbons. *Nature* **458**, 872–876 (2009)
85. Tapasztó, L., Dobrik, G., Lambin, P., Biró, L.P.: Tailoring the atomic structure of graphene nanoribbons by scanning tunnelling microscope lithography. *Nat. Nanotechnol.* **3**, 397–401 (2008)
86. Stampfer, C., Guttinger, J., Hellmüller, S., Molitor, F., Ensslin, K., Ihn, T.: Energy gaps in etched graphene nanoribbons. *Phys. Rev. Lett.* **102**, 056403 (2009)
87. Ci, L., Xu, Z., Wang, L., Gao, W., Ding, F., Kelly, K.F., Yakobson, B.I., Ajayan, P.M.: Controlled nanocutting of graphene. *Nano Res.* **1**, 116–122 (2008)
88. Campos, L.C., Manfrinato, R.V., Sanchez-Yamagishi, J.D., Kong, J., Jarillo-Herrero, P.: Anisotropic etching and nanoribbon formation in single-layer graphene. *Nano Lett.* **9**, 2600–2604 (2009)
89. Zhu, Z.P., Su, D.S., Weinberg, G., Schlogl, R.: Supermolecular self-assembly of graphene sheets: formation of tube-in-tube nanostructures. *Nano Lett.* **4**, 2255–2259 (2004)
90. Jin, W., Fukushima, T., Niki, M., Kosaka, A., Ishii, N., Aida, T.: Self-assembled graphitic nanotubes with one-handed helical arrays of a chiral amphiphilic molecular graphene. *Proc. Natl. Acad. Sci. USA* **102**, 10801–10806 (2005)
91. Chen, Q., Chen, T., Pan, G.-B., Yan, H.-J., Song, W.-G., Wan, L.-J., Li, Z.-T., Wang, Z.-H., Shang, B., Yuan, L.-F., Yang, J.-L.: Structural selection of graphene supramolecular assembly oriented by molecular conformation and alkyl chain. *Proc. Natl. Acad. Sci. USA* **105**, 16849–16854 (2008)
92. Lee, C., Wei, X., Kysar, J.W., Hone, J.: Measurement of the elastic properties and intrinsic strength of monolayer graphene. *Science* **321**, 385–388 (2008)
93. Bunch, J.S., Verbridge, S.S., Alden, J.S., van der Zande, A.M., Parpia, J.M., Craighead, H.G., McEuen, P.L.: Impermeable atomic membranes from graphene sheets. *Nano Lett.* **8**, 2458–2462 (2008)
94. Gómez-Navarro, C., Burghard, M., Kern, K.: Elastic properties of chemically derived single graphene sheets. *Nano Lett.* **8**, 2045–2049 (2008)
95. Viculis, L.M., Mack, J.J., Kaner, R.B.: A chemical route to carbon nanoscrolls. *Science* **299**, 1361 (2003)
96. Braga, S.F., Coluci, V.R., Legoas, S.B., Giro, R., Galvao, D.S., Baughman, R.H.: Structure and dynamics of carbon nanoscrolls. *Nano Lett.* **4**, 881–884 (2004)
97. Yu, D., Liu, F.: Synthesis of carbon nanotubes by rolling up patterned graphene nanoribbons using selective atomic adsorption. *Nano Lett.* **7**, 3046–3050 (2007)
98. Sidorov, A., Mudd, D., Sumanasekera, G., Ouseph, P.J., Jayanthi, C.S., Wu, S.-Y.: Electrostatic deposition of graphene in a gaseous environment: a deterministic route for synthesizing rolled graphenes? *Nanotechnology* **20**, 055611 (2009)
99. Martel, R., Shea, R.H., Avouris, P.: Ring formation in single-wall carbon nanotubes. *J. Phys. Chem. B* **103**, 7551–7556 (1999)
100. Huang, J., Juskiewicz, M., de Jeu, W.H., Cerda, E., Emrick, T., Menon, N., Russell, T.P.: Capillary wrinkling of floating thin polymer films. *Science* **317**, 650–653 (2007)
101. Py, C., Reverdy, P., Doppler, L., Bico, J., Roman, B., Baroud, C.N.: Capillary origami: spontaneous wrapping of a droplet with an elastic sheet. *Phys. Rev. Lett.* **98**, 156103 (2007)
102. Ellis, R.J., Vandervies, S.M.: Molecular chaperones. *Annu. Rev. Biochem.* **60**, 321–347 (1991)
103. Juniper, B.E., Robins, R.J., Joel, D.M.: *The Carnivorous Plants*. Academic, London (1989). ISBN 0-1239-2170-8
104. Lee, K.B., Park, S.J., Mirkin, C.A., Smith, J.C., Mrksich, M.: Protein nanoarrays generated by dip-pen nanolithography. *Science* **295**, 1702–1705 (2002)

105. Duwez, A.-S., Cuenot, S., Jérôme, C., Gabriel, S., Jérôme, R., Rapino, S., Zerbetto, F.: Mechanochemistry: targeted delivery of single molecules. *Nat. Nanotechnol.* **1**, 122–125 (2006)
106. Walther, J.H., Werder, T., Jaffe, R.L., Gonnet, P., Bergdorf, M., Zimmerli, U., Koumoutsakos, P.: Water–carbon interactions III: the influence of surface and fluid impurities. *Phys. Chem. Chem. Phys.* **6**, 1988–1995 (2004)